Strain-Field Based Segmentation for Fabric Formwork

Abhinit Sati, Tiffany Bao, Jeff Tedi, Edward Chien, Emily Whiting

Boston University, USA
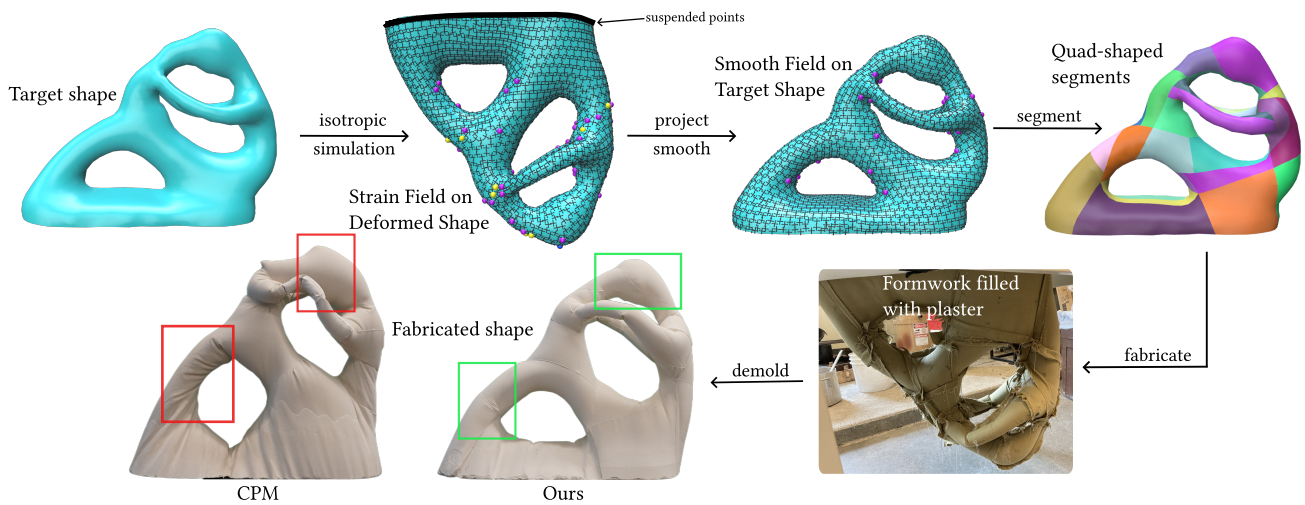
Figure 1: *Pipeline overview: We first simulate deformation of the mold under the load of the plaster infill (§3). Then we compute a strain field that captures local deformations on the mold. We project this field onto the target shape and smooth it (§4). A segmentation algorithm segments the target mesh into quad-shaped patches such that cloth fiber directions and seams align with the strain field (§6). The segments are flattened to the plane and used to trace fabric patches that can be sewn together to make the mold. The mold is filled with plaster, allowed to cure, and then demolded. Bottom Left: Comparison with the segmentation method from [PDF*22] (we refer to it as CPM, which is an automatic garment production system). Our approach yields fabricated shapes with better geometric fidelity.*

Abstract

We present a physically-informed segmentation pipeline for producing fabric formwork for the casting and molding of arbitrary 3D objects. Fabric formworks are molds made by stitching together patches of textile fabric. The mechanical flexibility offered by these molds aids the fabrication of unconventional and complex geometries and allows for greater transportation ease for on-site fabrication tasks. We employ an isotropic material model to estimate maximal strain directions that result when casting fluid is poured into the formwork. Our physically driven segmentation approach ensures seams and fiber directions align with these maximal strains. Experimental observations indicate that this alignment strategy significantly reduces twisting and shearing artifacts associated with the orthotropic deformation of woven fabrics. Aligning seams with strain directions further limits deformation of the formwork, improving fidelity to the input model. Moreover, our segmentation improves upon that of [ZFS*19] by promoting smoother seams and quad-like patches, reducing the time and expertise needed to construct the formwork. We validate the efficacy of our pipeline by fabricating and simulating shapes of varying complexity, showing superior geometric reconstruction and fabrication ease.

Keywords: Computer-Aided Manufacturing, Mesh segmentation, Fabric Formwork, Fabrication, Molding & Casting

1. Introduction

Recent computational mold-making methods enable hobbyists to fabricate intricate shapes [AMG*19, MPBC16], but these 3D-

printed molds face size limitations unsuitable for architectural-scale structures. Large-scale additive manufacturing approaches, such as those proposed by [Kho04] and [Bog13], involve significant technical complexities and high costs. To address this, [ZFS*19] introduced a computational pipeline for fabric-based molds, known as *Fabric Formwork*. These fabric containers, first realized during the industrial revolution [VWB11], are crafted by joining together flat patches of fabric to produce a three-dimensional mold. This helps circumvent size limitations and enables the fabrication of structures of arbitrary size and good surface quality at a low cost.

While [ZFS*19] developed a comprehensive computational pipeline for designing fabric formworks, their approach overlooked a key aspect. They optimized the geometry of the patches based on the physics of the deformation from the plaster infill via an inverse design approach. However, the initial patches were generated through a segmentation procedure focused solely on developability, which can result in poor initial guesses and cause the optimization to converge to suboptimal local minima. To address this, we propose a more physically driven segmentation pipeline in this work. Our segmentation method is self-contained and effective on its own, but can also serve as a good initialization for subsequent inverse design optimization.

We make the following observation based on our understanding of the material properties of woven fabrics. When designing fabric formworks, aligning fiber directions with strain directions is crucial, as woven fabrics typically have a low shear modulus (see Figure 2) and stretching along the bias leads to defects like twisting and shearing of the cloth mold [Gor09](Ch. 12) (Fig. 1). Proper fiber alignment also optimizes load distribution and prevents tearing of the formwork during the curing process [Wes16]. We estimate these strain directions using a non-linear isotropic material model and align fibers accordingly. Our findings show that this approach effectively minimizes asymmetric distortions caused by shearing, as the mold stretches primarily along the much stiffer warp and weft directions under fluid infill pressure. A more thorough discussion demonstrating this under perfect alignment can be found in Sec. 5.

We use this strain field to segment the mold into quad-shaped patches aligned with fiber directions. Tracing the orthogonal strain field yields patches whose seams align with maximal strain, further minimizing distortion due to increased stiffness. Quad-shaped patches also facilitate smooth seams, simplifying the sewing process. We validate our approach with the help of both physically fabricated and simulated results. We compare our results to other segmentation approaches from prior work on fabric formwork [ZFS*19], garment sewing patterns [PDF*22], and general purpose developable segmentation [SC18]. We demonstrate how fiber and seam alignment with strain directions improves the match to the target shape. In summary, our contributions include:

- A strain field synthesis procedure that captures local mold deformations and generates a vector field with high-quality topology, enabling the tracing of developable segments aligned with the strain field.
- A field-tracing-based segmentation method that aligns fibers and seams with, or orthogonal to, the directions of maximal strain—providing stiffness where needed and reducing torsion, twisting, and overall distortion in the formwork.
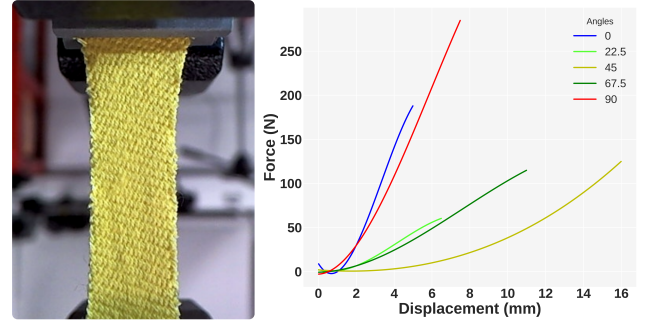

Figure 2: *Left: Fabric sample stretched in tensile testing at a bias of 45 degrees, Right: Tensile test force-displacement data for various bias angles.*

- A merging approach resulting in patches that are easier to sew due to their quad-like nature and smoother boundaries, facilitating the fabrication process.

2. Related Work

2.1. Cloth-based Inverse Design

Past work in inverse design has largely employed iterative optimization based approaches. In this section, we review some of these works and highlight their key limitations. [LCBD*18] proposed an inverse-design framework to estimate the rest shape of thin shells and the frictional contact forces required to achieve a target deformation. However, their simulation models each mesh edge as a spring with constant stiffness, which—as shown by [MBT*12]—fails to accurately capture in-plane shearing behavior. [LDW*22] proposed a differentiable cloth simulation pipeline, enabling inverse tasks such as material calibration and trajectory planning. Rod and plastic-reinforced, pre-stretched fabrics are optimized to deploy into a target shape in [POT17] and [JSVB22] respectively, while [MTMP20] reduce seam stress and pressure for skin-tight garments. All three aforementioned works assume isotropic cloth, even though real fabrics are typically orthotropic. These approaches also require computing force Jacobians, which are particularly difficult to evaluate for non-linear orthotropic fabric models, as demonstrated by [FWYX24]. It should also be noted that a good initial guess is crucial, as these optimizations operate over highly non-convex landscape with many local minima. State-of-the-art approaches for differentiable cloth simulation such as [LLK19] suffer from the same issues - they simplify the stiffness model from [WOR11] to an isotropic one and struggle to estimate stiffness values for large deformations accurately for the material parameter estimation task.

2.2. Computational Mold Design

Many advances in algorithms and computational approaches for the fabrication of free form shaped 3D structures have been seen in recent years. [AMG*18] demonstrate a segmentation technique to fabricate metamolds - intermediate 3D printed molds used for casting silicone molds. These silicone molds can then be used to create multiple copies of the desired 3D object. In a similar vein, the algorithms developed by [VLAR19] enable the fabrication of multi-

material objects. [SJG19] deform an input 3D object to make it fabricable via a 2-piece mold. [AMB*21] enable the fabrication of very complex 3D shapes by segmenting them into individual pieces that can each be produced via a 2-piece mold, and then joined together to form the final geometry. A comprehensive survey of the works is outlined in [AMA*22].

2.3. Developable and Quad-Layout based Mesh Segmentation

Several mesh segmentation algorithms tackle a range of challenges for optimizing patch and seam properties. [MS04] use strip-based approximation methods to create papercraft models out of flat sheets of paper. Piecewise-developable remeshing techniques approximate curved regions by locally developable ones, easing flattening and segmentation [SGC18, IRHSH20, ZFO*22, WZZ*23, BPT*25]. The aforementioned algorithms focus only on curvature reduction and quite often produce segments having intricate boundaries. [Wan07] segment via a boundary-length preserving 2D parameterization, but the resulting jagged patch borders complicate fabrication. [PDF*22] tailor garments with developable patches, but their input model symmetry assumption yields highly asymmetric patches for meshes with no planes of symmetry. [GSV*17] produce compact 3D curve-networks for a given surface that could potentially also be used for extracting a quad-layout segmentation.

[Cam17] gives a comprehensive survey of the state of the art in quad-layout based segmentation techniques. A quad layout is advantageous since it mitigates the challenges associated with the papers described above and generates simple to sew 2D patches upon parameterization. Our quad-layout segmentation approach is inspired by the work of [PPM*16] and [LCK21]. The former addresses a graph planning problem, tracing a network of separatrices that follow an input vector field on the mesh to partition it into segments. Meanwhile, the latter relaxes singularities in the input vector field used to inform the segmentation, thereby simplifying the resulting segmentation.

2.4. Physically Informed Field-Driven Fabrication

[VZF*19] design a geodesic field on the 3D input surface for informing a fabricable triaxial weave structure to reproduce the given geometry. [SB10] and [PTP*15] both use strain and stress fields to inform the layout of grid shells for improving the load bearing capabilities of architectural structures. [AJL*19] and [SOG*22] produce topology optimized structures from a stress field computed from FEA and from an input frame field respectively. The former smooths piecewise constant stress fields and applies frame field optimization to handle degenerate cases—similar to our isotropic scenario (see 4.2.2)—yielding a stress-aligned parameterization for truss generation. The latter categorizes field singularities into isotropic regions (due to non-unique microstructure orientations), solid regions (fully filled, orientations irrelevant), and voids (no material). They eliminate spurious singularities in isotropic regions using a regularization procedure described in [GSA*20], and terminate streamline tracing in solid/void regions. In partially filled regions, standard streamline (tangent curve) tracing is used. The field smoothing approach in [AJL*19] achieves a similar outcome to

ours by interpolating the frame field from well-defined anisotropic regions into ill-defined isotropic ones. However, their method eliminates singularities to enable a global parameterization, while we retain them to guide segmentation cuts on the 3D shape.

3. Simulation Model

We begin by establishing our simulation model and notation. Our system takes a target shape $\hat{\mathbf{X}} \in \mathbb{R}^{3N}$, discretized by vertices $\hat{\mathbf{x}}_{\mathbf{i}} \in \hat{\mathbf{X}}(i = 1, ..., N)$, as input. We represent the flat fabric panels, parameterized in 2D material coordinates as $\mathbf{X} \in \mathbb{R}^{2n}$, discretized by vertices $\mathbf{x}_{\mathbf{i}} \in \mathbf{X}(i = 1, ..., n)$. It is important to note that $n > N$, since a vertex on the target shape can be shared by more than one flat panel (in the case of seams).

The deformed shape at force equilibrium is represented as $\overline{\mathbf{X}} \in \mathbb{R}^{3N}$, discretized by vertices $\overline{\mathbf{x}}_{\mathbf{i}} \in \overline{\mathbf{X}}(i = 1, ..., N)$. We obtain the mold equilibrium shape with the help of the cloth simulation model described below.

3.1. Non-linear Isotropic Material Model

We propose using a non-linear isotropic material model for simulation, which removes the need for directional stiffness assumptions and treats all directions uniformly. To capture the strain-limiting behavior typical of fabrics, we define the stiffness tensor as a function of the Green strain tensor $\boldsymbol{\varepsilon}$ (Eq. 3), formulated as follows:

$$\mathbf{K}(\boldsymbol{\varepsilon}) = \begin{bmatrix} k_{uu}(\boldsymbol{\varepsilon}) & k_{uv}(\boldsymbol{\varepsilon}) & 0 \\ k_{uv}(\boldsymbol{\varepsilon}) & k_{vv}(\boldsymbol{\varepsilon}) & 0 \\ 0 & 0 & k_{ss}(\boldsymbol{\varepsilon}) \end{bmatrix} \qquad (1)$$

We set the stiffness values along the longitudinal and transverse axes to be the same, i.e $k_{uu} = k_{vv}$. We then employ the following expression for isotropic materials, which establishes a relationship between longitudinal and transverse stiffness, Poisson's ratio, and shear stiffness, derived from Lamé's second parameter equation [Lov13]

$$k_{ss} = \frac{k_{uu}}{2(1 + k_{uv})} \qquad (2)$$

We elaborate more on the values we choose for these material parameters in Supp. Sec. 11.

We use this isotropic material model to estimate strain directions despite the orthotropic nature of woven fabric (Sec. 4). A simple example motivates this and shows why the isotropic simulation can still recover strain directions accurately. Consider two rectangular fabric samples: one with warp and weft aligned to the edges and one rotated by 45°. Under horizontal uniaxial stretch, both exhibit the same maximum strain direction (horizontal) even though their stretch magnitudes differ. With fiber misalignment, strain directions change only modestly, while shearing (sometimes leading to twisting) increases substantially as shown throughout in our results (Sec. 7).
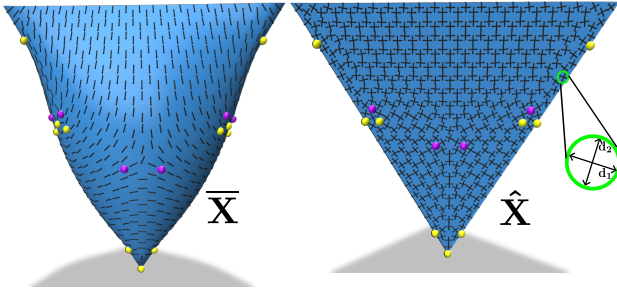
Figure 3: *Strain Field on a tetrahedron mesh. Left: Larger stretch directions capture how the fabric mold deforms - vertically near the top and horizontally as we near the bottom to produce the equilibrium shape in this example. Right: Both principal stretch directions after projecting them to the rest shape. Yellow spheres denote valence 3 singularities and Purple ones denote valence 5 singularities. $\overline{\mathbf{X}}$ - deformed shape, $\hat{\mathbf{X}}$ - target shape. $\mathbf{d_1}$ and $\mathbf{d_2}$ denote the transformed stretch directions.*

3.2. Forces

In this subsection, we briefly describe the computation of forces used to determine the equilibrium shape, which is subsequently used to compute the vector field described in §4. These forces are of two types: membrane forces that describe the tension within the cloth, and plaster infill forces.

We model membrane forces as the gradient of the non-linear StVK stretch energy [SSBL*22] and plaster fluid forces using the approach of [ZFS*19]. We are interested in the shape we can obtain when the fabric formwork is at equilibrium with the fluid pressure from the plaster infill. This implies that our system is at rest and all the forces at all points on the deformed shape $\overline{\mathbf{X}}$ must cancel each other out. The exact computation of the forces and their Jacobians used for the backward Euler solver [BW23] is detailed in Supp. Sec. 3.

4. Local Deformation Vector Field

We compute a 4-vector field [VCD*16] on the mesh that captures the local deformations the fabric container undergoes when it deforms under the load of the plaster infill. We will see how this vector field guides the orientation for the fabric patches and the resulting seams between them in §6.

4.1. Vector Field Synthesis

Let the cloth simulation program be a function P that maps the flat panels in 2D: $\mathbf{X}$, to the deformed mesh in 3D: $\overline{\mathbf{X}}$. We can then define $P : \mathbf{X} \to \overline{\mathbf{X}}$. This means that every triangle representing the flat panels in 2D will get mapped to a corresponding triangle on the deformed mesh in 3D. Since we do not know what the flat panels are initially, we flatten every triangle of the 3D target shape isometrically to the plane. The transformation can then be obtained by computing the deformation gradient $\mathbf{F}$, which gives the per-face Jacobian of the piecewise-linear mapping P of the 2D patches into deformed 3D space [KE20].

We characterize the mold's in-plane deformation locally using

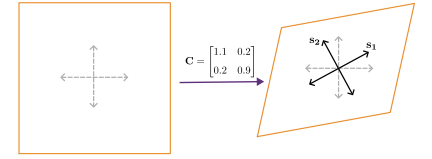the Cauchy-Green deformation tensor, defined as follows

$$\mathbf{C} = \mathbf{F}^T \mathbf{F} = 2\boldsymbol{\varepsilon} + \mathbf{I} \tag{3}$$

This tensor helps us measure the in-plane stretching and shearing on every triangle element in the mesh, independent of the rotation that element had to undergo during deformation. To further analyze the stretching behavior, we decompose $\mathbf{C}$ as follows

$$\mathbf{C} = \lambda_1 \mathbf{s_1} \otimes \mathbf{s_1} + \lambda_2 \mathbf{s_2} \otimes \mathbf{s_2} \tag{4}$$

λ_1 and λ_2 are the principal stretch values squared, which describe the magnitude of stretching along the directions $\mathbf{s_1}$ and $\mathbf{s_2}$ respectively. $\mathbf{s_1}$ and $\mathbf{s_2}$ describe the directions of maximum and minimum stretch respectively (assuming $\lambda_1 \geq \lambda_2$, see Fig. 3).

The inset figure gives an example of simultaneous stretching and shearing an element can undergo. It shows how a rest shape deforms under the action of $\mathbf{C}$. $\mathbf{s_1}$ and $\mathbf{s_2}$ depict the rotation and stretching of the canonical axes in gray. To express these stretch directions on the target 3D shape, we transform them by $\hat{\mathbf{F}}$ as follows

$$\mathbf{d_1} = \hat{\mathbf{F}} \mathbf{s_1} \tag{5}$$

$$\mathbf{d_2} = \hat{\mathbf{F}} \mathbf{s_2} \tag{6}$$

We then define the 4 vectors that make up the 4-vector field as follows: $\mathbf{d_1}, -\mathbf{d_1}, \mathbf{d_2}, -\mathbf{d_2}$ (see Fig. 3, right). The transformation matrix $\hat{\mathbf{F}}$ maps $\mathbf{s_1}$ and $\mathbf{s_2}$ from the 2D rest triangles $\mathbf{X}$ to the target shape in 3D $\hat{\mathbf{X}}$ (see Fig. 3, right). This matrix represents the Jacobian of the piecewise linear mapping of the 2D patches into target 3D space and is computed similarly to the deformation gradient described before. Due to the isometric mapping in 2D, it preserves orthogonality between the strain field vectors after transformation. In a similar vein, we can use the deformation gradient $\mathbf{F}$ to transform the strain directions in 2D to the deformed shape (Fig. 3, left).

4.2. Field Smoothing

The strain field synthesis procedure described above has a tendency to produce fields that are noisy and asymmetric. The overall field has structure and symmetry that can be seen visually, but that isn't captured by the field topology, i.e., by positions of the singularities (see Fig. 4, left). This is especially true in regions where $\lambda_1 \approx \lambda_2$, and the principal stretch directions may be ambiguous and unstable. [AJL*19] tackle this problem by estimating frame field vectors that best align with the input stress field, followed by a smoothing operation using the cotan-Laplacian matrix.

In our approach, we begin by labeling certain regions on the mesh as *isotropic*, when local stretch values of the vector field are roughly equal, i.e $\lambda_1 \approx \lambda_2$, and *anisotropic* otherwise. We then introduce two field smoothing procedures designed to denoise the overall field and promote field simplicity.
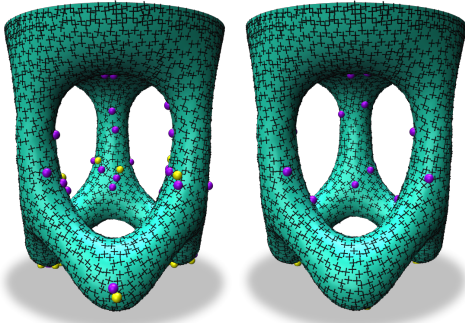
Figure 4: *Left: Original field (noisy in some regions), Right: Smoothed field after minimizing the energy in Equation 7 with α = 0.5 ensures a good balance between alignment to the original field and smoothness.*

4.2.1. Field Smoothing for Denoising

For the first smoothing procedure that reduces overall noise, we want to maintain a balance between smoothness and the alignment to the original field for all regions on the mesh - both *isotropic* and *anisotropic*. To accomplish this, we modify the original smoothness energy described by [BZK09] and integrate soft constraints for following the original vector field defined as follows

$$E_{smooth}(\theta) = \underbrace{\sum_{e_{ij} \in E} \left(\theta_i - \theta_j + \kappa_{ij} + \frac{\pi}{2} p_{ij}\right)^2}_{\text{smoothness term}} + \alpha \underbrace{\sum_{f_k \in F} \left(\theta_k - \theta_k^t\right)^2}_{\text{soft constraint}} \quad (7)$$

For more details on this energy and the various terms in it, we urge the reader to refer to Supp. Sec. 4 and [BZK09].

4.2.2. Field Smoothing for Simplicity

To develop the next smoothing procedure that promotes field simplicity, we begin by analyzing how singularities arise in the strain field. By definition, a singular vertex is a vertex around which the field is non-smooth, i.e the 4-vector field rotates by at least $\frac{\pi}{2}$ radians. We observed that singular vertices are located within *isotropic* regions (see Fig. 5). When both eigenvalues are equal, the eigendecomposition of **C** becomes non-unique, allowing any pair of orthogonal eigenvectors to define the local strain field. This leads to non-smoothness in the field. In contrast, *anisotropic* regions yield a well-defined field that provides a more accurate measure of deformation.

Therefore, to further smooth the field, we maintain the same strain directions in *anisotropic* regions (specified as hard constraints) and solve for the smoothest possible directions in *isotropic* regions by minimizing the energy in equation 7, setting α = 0 (Fig. 5). Field smoothing offers several benefits: it reduces noise, merges clustered singularities, and improves overall structure. By relocating some singularities to high-curvature regions, it also promotes developable segments.
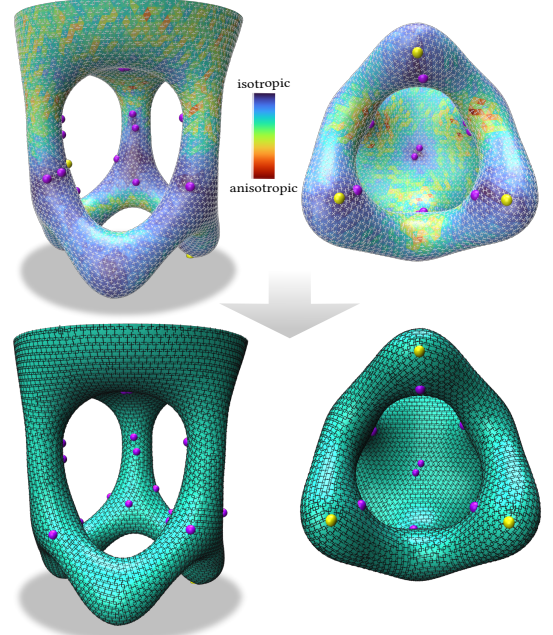

Figure 5: *Example showing a highly-tessellated table mesh and the corresponding vector field. Top: Plot depicting the absolute difference in stretch values $|\lambda_1 - \lambda_2|$ for the vector field post first round of smoothing (singularities differ slightly from Fig. 4 due to the denser triangulation), Bottom: A simpler vector field post second round of smoothing.*

5. Optimal Fiber Alignment with Strain Field

In this section, we explain why warp/weft fiber and strain field alignment is important for segmentation. We consider an idealized scenario in which the fiber material axes are perfectly aligned with the strain field. This ensures shearing strains vanish, helping us eliminate large deformations. Although this is nearly impossible to achieve in practice due to the curvature and topology of 3D objects, it provides a rationale for aiming to maximize this alignment.

Let **F** be the deformation gradient and $\mathbf{C} = \mathbf{F}^T\mathbf{F}$ be the right Cauchy-Green deformation tensor. Let $\mathbf{m}_1$ and $\mathbf{m}_2$ be the orthonormal warp-weft material frame reference configuration. We can quantify shearing in the material frame using the mixed term [Ogd97]

$$\varepsilon_{uv} \propto \mathbf{m}_1^T \mathbf{C} \mathbf{m}_2.$$

This quantity measures how much stretching along one material direction affects the other. Intuitively, **C** describes the local *strain ellipse* - it has two orthogonal directions along which deformation is purely extensional (no coupling), i.e., the principal strain directions. If we choose the material axes to coincide with these principal directions, then **C** becomes diagonal in the $(\mathbf{m}_1, \mathbf{m}_2)$ basis. In that case, the off-diagonal coupling (shearing) term vanishes,

$$\mathbf{m}_1^T \mathbf{C} \mathbf{m}_2 = 0$$

A more detailed proof is provided in the Supp. Sec. 5.

As we will see in the next section, the segmentation also ensures seams are aligned with the strain field. Seam alignment further minimizes distortion due to their increased stiffness.

6. Tracing and Segmentation

In the preceding section, we explored the process of computing and smoothing a 4-vector field that characterizes the local stretching experienced by the fabric container. In this section, we will use this vector field to perform a segmentation of the target shape that needs to be fabricated.

6.1. Segmentation via Path Tracing

We treat the segmentation problem as a graph path tracing problem, where the nodes of the graph are defined by the singularities and the edges are defined by the arcs connecting them. The resulting arcs partition the mesh surface into segments. These arcs are approximate separatrices of the underlying deformation vector field [Cam17]. We solve this problem by employing an approach similar to [PPM*16]. To find the optimal approximate separatrix emanating from a singular vertex, we solve a planning problem that traces a path on the surface of the mesh, seeking alignment with the local vector field to the greatest extent possible, while also keeping the length in check. We modify the cost function from [PPM*16] to penalize a path drifting away from the vector field, more details for which can be found in Supp. Sec. 6.

We trace separatrices starting from all singular nodes and terminate them when they reach another singular node, the boundary of the mesh or if they intersect another separatrix at an approximately 90 degree angle to form a T-junction (see inset figure).
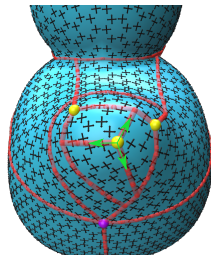
The topology of the graph hence depends on the order of separatrix tracing. However, the quality of the fabricated result remains largely unaffected, as the resulting segments are still quad-shaped with seams aligned to strain directions. Thus, we use a random tracing order.

6.2. Fabrication Complexity

Previously, we explored the process of faithfully tracing paths that align with the vector field. The resulting segmentation may produce numerous segments, potentially containing non-smooth boundaries. This in turn makes fabrication challenging. The following subsection outlines our strategies for simplifying the formwork fabrication process and reducing sewing time.

6.2.1. Seam Smoothness

Since we use mesh vertices to sample all nodes for the paths we trace, the resulting paths may not consistently exhibit a high level of smoothness. This discretization artifact can be mitigated by applying path smoothing through the computation of smooth
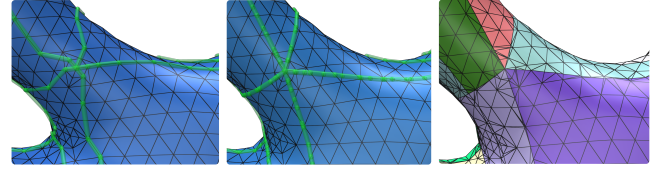

Figure 6: *Smoothing jagged paths. Left: Separatrices traced by the algorithm, Middle: smoothed separatrices, Right: remeshing along the newly smoothed separatrices for extracting patches with smooth seams.*
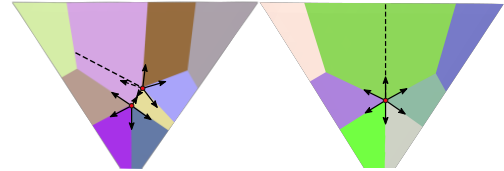

Figure 7: *Two valence 5 singularities close to each other are combined to create one valence 6 singularity. This results in fewer segments being created and eases fabrication complexity. Dotted lines indicate a former seam between 2 adjacent segments that were merged together.*

geodesic paths (Fig. 6), following the method described in [SC20]. This helps ensure the resulting seams between adjacent segments/patches in the fabric formwork are smooth and hence are easier and faster to sew.

### 6.2.2. Combination/Removal of Singularities

Inspired by the approach proposed by [LCK21], we relax singularities that are in the vicinity of each other. This process greatly simplifies the resulting segmentation by promoting the creation of fewer segments. The field rotations accumulate when two singularities are taken into account together. We can thus replace two valence 5 singularities with a valence 6 singularity (Fig. 7), without compromising on how well the traced separatrices follow the vector field. Similarly, a valence 5 singularity can cancel the rotation from a valence 3 singularity, allowing for the convenient removal of both. For more information on the singularities of 4-vector fields, see Supp. Sec. 7 and [VCD*16].

6.2.3. Developability

Our vector field smoothing concentrates singularities in high-curvature regions, promoting nearly developable segments. When segments still exhibit high curvature, we split them to reduce it. Through empirical observations, we have discovered that strategically splitting such segments into two distinct components yields a significant reduction in the overall curvature, thereby ensuring all patches created by the segmentation process are quasi-developable.

We employ the covariance energy formulation proposed by [SGC18] to measure the developability of a segment on a per vertex basis. Given the energy values we compute on a per vertex basis, we find an optimal cut to partition the segment into two and ensure the two new segments have minimal curvature. We utilize spectral clustering [VL07, NJW01] to partition a non-developable segment into k segments ($k = 2$).

The goal is to ensure, with high probability, that cuts are made along high-energy regions of the segment. The edge weights in the affinity matrix are set to represent this probability. The detailed steps for this process are described in the Supp. Sec. 8. The inset figure shows an example cut to split a segment.
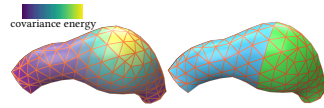
6.3. Patch Extraction

After tracing is complete and a valid segmentation is produced, each of the segments are flattened to the plane conformally using BFF [SC17] to obtain 2D patches for the formwork creation. BFF produces flattenings with very low area distortion and near-conformal angles which helps preserve candidate warp/weft orthogonality. While not guaranteed by the conformal parameterization, the boundaries (seams) of adjacent patches empirically maintain the same lengths, since our segments are quasi-developable. This ensures they are easy to sew.

6.4. 2D Patch Orientation

We orient the 2D patches obtained from conformal flattening to optimally align their interior and boundaries with the fiber directions using the following heuristics. We align the longest side of the patch with one of the two fiber directions and found it to be a good strategy since the warp and weft have similar stiffness (Fig. 2). For a patch where all sides are roughly the same length and are not at right angles to each other, we choose a different strategy. The patch is oriented such that the angles each side makes with the warp or weft directions (depending upon which is closer) is minimized. An example orientation of patches can be seen in Fig. 8.

7. Results and Validation

In this section, we outline the fabrication pipeline and present both fabricated as well as simulated results to validate our segmentation approach.

7.1. Fabrication Pipeline

Following is a step-by-step description of our fabrication pipeline for crafting fabric formwork. Our pipeline is inspired by [ZFS*19], with some key modifications tailored to our specific requirements, such as orienting the 2D patches in the warp/weft plane to align with fiber directions (Fig. 8).

(A) We orient the 2D patches to cut the fabric pieces based on the procedure described in §6.4.
(B) The patches are sewn together to create the formwork. The formwork is then clamped to a rigid frame at specified suspension points.
(C) Liquid casting material is poured into the openings of the formwork. The infill material is allowed to cure and solidify. We use plaster of Paris powder mixed with water in a 1:1 ratio.
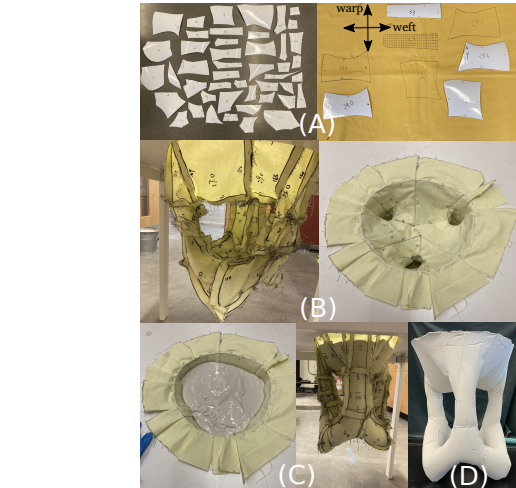(D) The cloth panels are removed to unveil a robust, cast plaster prototype.

Figure 8: *Fabrication pipeline. (A) Cut patches and orient them w.r.t to the warp/weft directions (B) stitched formwork suspended to a frame (C) formwork filled with liquid plaster (D) Demolded object after curing is complete*

In our experiments, we use suspension orientations **d** computed by [ZFS*19] for the table, elephant, chair and fertility models and don't optimize it separately. For the tetrahedron and hand models, we pick an orientation manually. $\rho = 1460$ kg/m^3 is the density of liquid plaster prepared for the infill and we use the same value in our simulations.

7.2. Comparisons with other Methods

We validate our approach by comparing fabricated and simulated results generated from our segmentation pipeline with those produced by three alternative methods - *Computational Pattern Making from 3D Garment Models* (CPM) [PDF*22], *Computational Design of Fabric Formwork* (CDFF) [ZFS*19] and *Variational Surface Cutting* (VSC) [SC18]. Although CPM and VSC are not specifically designed for fabric formworks, the comparisons highlight why incorporating system physics is essential—and why purely geometric segmentation falls short.

CPM generates sewing patterns to create garments from input 3D models and isn't designed to account for the force scenarios inherent in fabric formwork. It segments meshes into quad patches by tracing separatrices along principal curvature directions. CPM differs from our method in two key ways: (1) field singularities may lie within patches, preventing warp/weft and seam alignment with strain directions (see Fig. 9, top row; Fig. 13); and (2) segmentation symmetry is enforced via a bilateral plane, limiting applicability to shapes with exact symmetry (Fig. 9).

CDFF is explicitly aimed at designing fabric formworks and combines the approaches from [CSAD04] [Wan07] to get an initial developable segmentation. An inverse design approach is then used to optimize this segmentation to best match the target shape. Because the initial segmentation is driven purely by geometry and doesn't account for the underlying physics, it is likely suboptimal, and the subsequent optimization may be unable to fully compensate. Our method works well in a stand-alone fashion, but may also
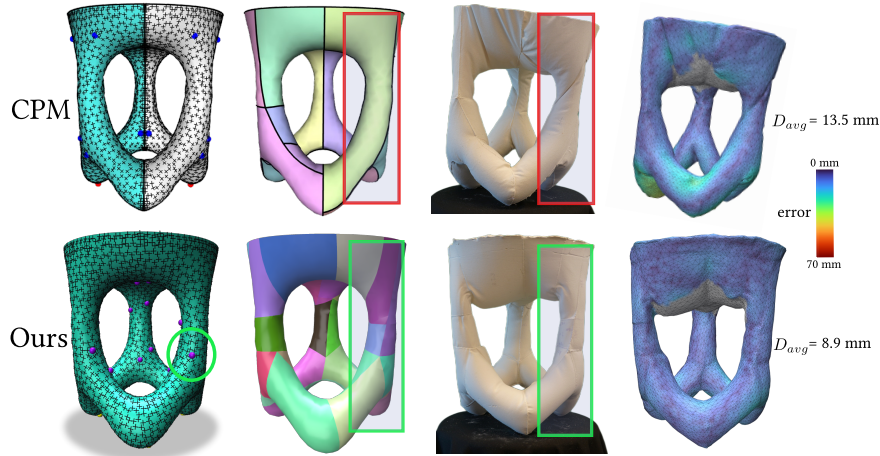
Figure 9: *Comparison of results from using the segmentation pipeline in CPM [PDF*22] (top) with our approach (bottom). Red rectangles highlight twisting in the fabricated model. From left to right - Vector Field used for segmentation (curvature field for CPM and strain field for ours), Final Segmentation, Fabricated result, Scanned model of the fabricated result. D_{avg} shows the average deviation from the target. We gray out regions on the scanned model where supports would be placed to prevent sagging.*
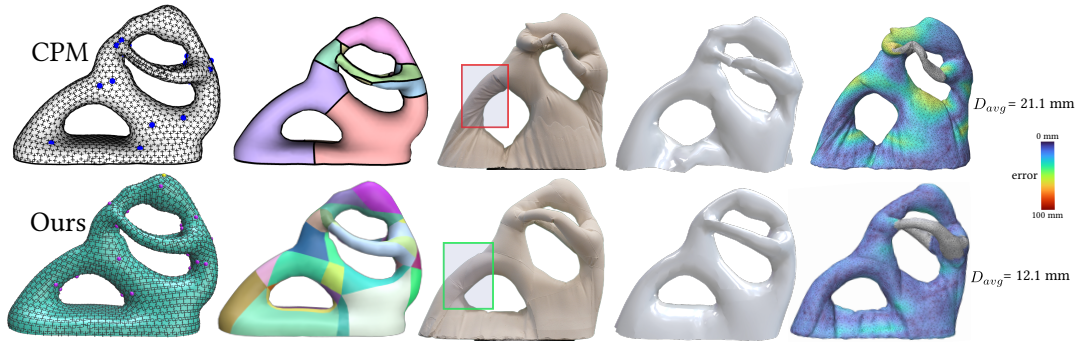

Figure 10: *Comparison of results from using the segmentation pipeline in CPM [PDF*22] (top) with our approach (bottom). (Left to right) Vector field used for segmentation (curvature field for CPM and strain field for ours), Final Segmentation, Fabricated result, Simulated result with the full orthotropic cloth model, Scanned model of the fabricated result. D_{avg} shows the average deviation from the target. Again, the red rectangle (top) highlights twisting in the fabricated model. We gray out regions on the scanned model where supports would be placed to prevent sagging.*

be considered as an initialization for the inverse patch optimization of CDFF. We also point out that the 2D patches generated by CDFF often have irregularly shaped boundaries, complicating subsequent stitching and fabrication (eg. the table model in Fig. 11). Lastly, we note that our comparisons to CDFF are qualitative as the code for the method is not open-source.

VSC is a developable segmentation approach that takes an input embedded graph and optimizes it for a balance between seam length and distortion of individual segments when flattened conformally. While principled, this purely geometric approach is also not purpose built to account for the physical conditions fabric formworks experience. In our comparison implementation, we utilize D-charts [JKS05] for the initial segmentation.

7.3. Fabricated Models – Fertility and Table

We scan the fabricated models using an iPhone 15 LiDAR sensor with the Kiri Engine 3D app and align them to the target models using the Iterative Closest Point (ICP) method [RBB09, CZK15]. We compute the closest-point distances from the scans to the targets (rightmost images in Figs. 9 and 10). When compared to CPM, our segmentation yields fabricated models that more closely match the target, both visually and by average per-vertex deviation from the scan.

Methods like CPM and CDFF exhibit limitations that affect fabrication quality. Because the strain field rotates within some patches, these methods introduce shearing and twisting artifacts (Fig. 9 and Fig. 11). Misalignment between the strain field and fiber directions further exacerbates deformation, causing excessive
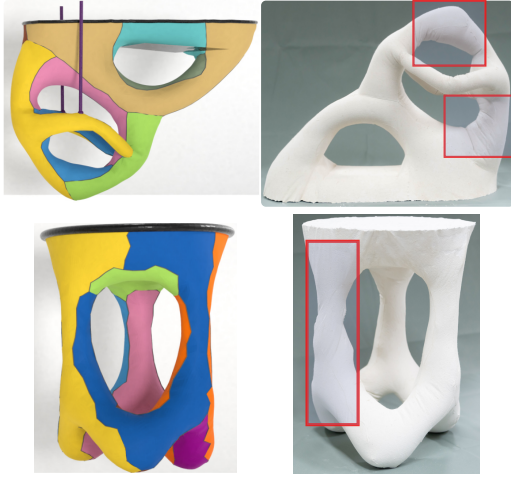
Figure 11: *Fertility model (top) and Table model (bottom) from CDFF, images reprinted from [ZFS*19]. Red boxes highlight the wrinkling and twisting artifacts on the fabricated models.*
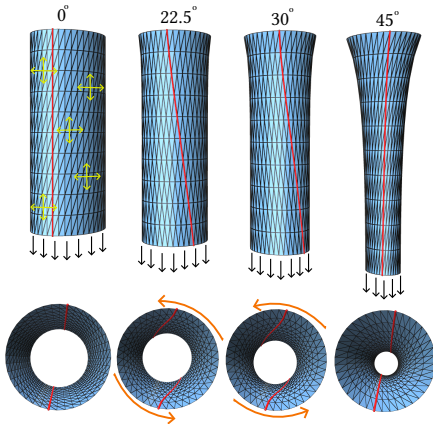

Figure 12: *Cylinder model being pulled on the bottom ring with a force of 250 N. Black arrows indicate the direction of forces. From left to right: The effect of orienting 2D patches that form the curved surface at various bias angles. Top and Bottom: Front on view and top down view of the model respectively. Orange arrows indicate twisting of the cylinder for bias angles 22.5 and 30. The strains are indicated by yellow crosses. Seams are indicated in red.*

stretching and bulging (Fig. 10, top row). In contrast, our approach addresses these issues by aligning seams and fibers with a well structured strain field, producing fabricated shapes with minimum distortion. As a result, the fabricated shapes more closely match the intended geometry (Fig. 9 and 10, bottom row).

Unlike the CDFF approach, we did not incorporate additional supports during fabrication, as this was beyond the scope of our investigation. This led to sagging on the underside of the table and the fertility model's arms. However, our simulation and field smoothing framework can readily accommodate such additions if needed, as we have done for the chair model described in the next subsection.
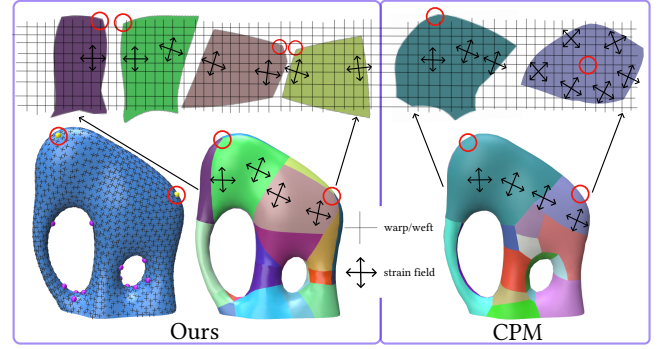

Figure 13: *Patch orientations with respect to warp/weft (grid) and strain field samples (crosses) on the model and 2D patches. Left: Our approach produces quad-shaped patches, enabling better alignment of the strain field with the warp/weft. Right: Irregularly shaped patches from CPM. CPM also produces patches with strain field singularities in their interior (red circles in patches on the right), making good alignment over the whole patch impossible.*

The inset figure shows the chair model at rest on the left, and its deformed counterpart at equilibrium on the right with four plane supports.

7.4. Simulated Results

In this subsection, we present simulated results obtained from non-linear orthotropic simulations. We use the non-linear orthotropic material model from [WOR11], fitting its parameters to match simulated force-displacement curves with experimental data from Instron tensile tests (see Supp. Sec. 10 for details).

7.4.1. Simulated models - Cylinder, Chair, Elephant and Hand

To further highlight the importance of fiber alignment with strain directions, we simulate a cylinder model under simple loading conditions. The cylinder is subject to downward vertical forces as shown in Fig. 12. We segmented the mesh into two patches, orienting them to vary fiber angles relative to the main vertical strain directions. Due to asymmetric shearing and material orthotropy, significant twisting occurs in models with patch orientations of 22.5° and 30° (Fig. 12). At 45°, deformation is greatest but twisting is absent. The 0° patch orientation produces the best match to the target, as the strains and the fiber directions are in perfect alignment.

For the chair model, we use plane supports as in [ZFS*19] (inset figure in Sec. 7.3), which help limit deformation across all three methods (Fig. 14). However, the VSC and CPM approaches show sagging at the top of the chair's backrest and along the seat edges (Fig. 14, top row). In the elephant model, both methods produce major distortions near the head, where infill pressure is highest. Our strain-guided quad-layout segmentation aligns seams better with the strain field (Fig. 13) in contrast to CPM, which often produces patches where the strain field rotates in the interior of the patch, causing large deformations. In the hand model, our approach preserves finger shape without extra support, while VSC and CPM
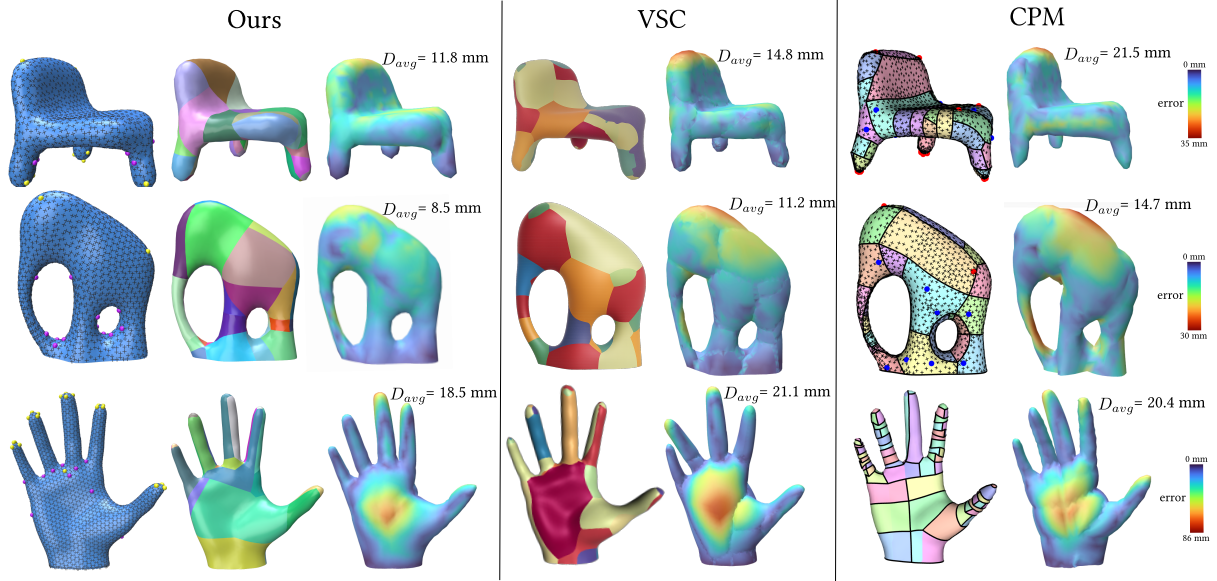
Figure 14: *From left to right: strain field produced with our vector field smoothing approach, our shape segmentation, simulated results from our segmentations, shape segmentation using the approach of VSC, corresponding simulated result, shape segmentation using the approach of CPM, corresponding simulated result with deformations normalized and visualized as color maps. D_{avg} shows the average deviation from the target.*

yield thicker, shorter fingers due to stretching and compression from the Poisson effect. This highlights that accurate shape reproduction depends more on proper seam and fiber alignment than simply increasing the number of patches (CPM uses 80 patches for the hand model; see Fig. 14, bottom right). In the VSC and CPM results, misalignment between strain and seam directions causes excessive stretching, leading to outward bulging made more prominent due to the really stiff seams (Fig. 14, middle and bottom row).

Table 1: *Design configurations for different models: number of patches (subdivided by all methods), supports used, and average time for our method.*

Model	Patches			Supports	Time (s)
	Ours	**VSC**	**CPM**		**Ours**
Table	33	-	17	None	65
Fertility	30	-	15	None	62
Chair	35	37	35	4 planes	312
Elephant	36	40	37	None	53
Hand	30	39	80	None	107

Table 2: *Strain Field deviation comparison across methods.*

	Median Deviation in Degrees		
Model	Ours	VSC	CPM
Chair	11.74	11.44	9.45
Elephant	13.74	12.60	11.63
Hand	8.94	8.95	15.65

We show strain directions computed with both the isotropic and orthotropic material models in the simulation for the elephant mesh (see Fig. 15). The comparison highlights how strain directions remain the same qualitatively and do not change much between the
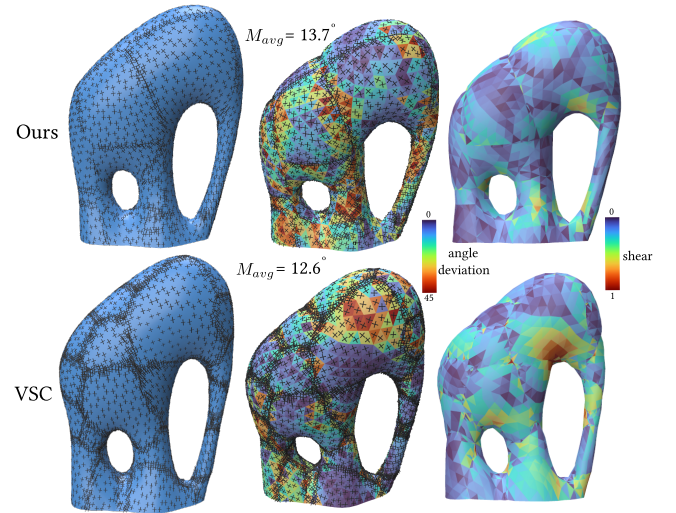

Figure 15: *Strain directions comparison. Left: Strain field computed from the isotropic simulation. Middle: Strain field computed from the orthotropic simulation. Right: Normalized shearing computed from the right CG tensor **C** (Eq. 3). M_{avg} shows the median deviation of the orthotropic strain field from the isotropic one. The isotropic simulation was run with the mesh produced by the respective segmentation methods (that remesh a lot along the seams) for ease of comparisons with the orthotropic strain field.*

isotropic and orthotropic models (see Table 2 for more data). However, the resulting stretching and deformation depends a lot on how well the seams and fiber directions are aligned with the strain direc-
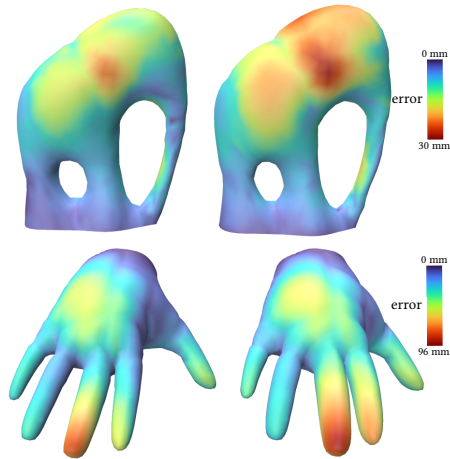
Figure 16: *Effect of warp/weft alignment. Left: Optimized seam positions and patch orientations. Right: Optimized seam positions but 2D patches rotated by 45 degrees. Error from the target shape is noticeably larger.*

tions. The misalignment between the two in the VSC result means that we see much higher levels of shearing and distortion. In the third column of Fig. 15, we visualize the normalized shear experienced by each triangle element under our method and VSC. Perfect alignment of seams and fibers with the strain field is challenging due to the model's varying curvature, yet our method consistently achieves lower shear, resulting in reduced deformation and a closer match to the target shape.

We also demonstrate that the alignment of both seams and fiber directions in the interior of the 2D patches is crucial for accurate shape estimation. Fig. 16 helps showcase how rotating patches by 45 degrees to their optimal orientation results in larger deformations. We keep the (optimized) seam positions the same in this comparison.

8. Conclusion

In this work, we introduced a segmentation approach for fabric formwork that considers the orthotropic properties of the fabric and its impact on deformations caused by the plaster infill, ensuring the solidified structure closely aligns with the target shape. We compute a vector field that accurately captures local deformations in the formwork and developed a segmentation algorithm to leverage this field, helping us minimize artifacts caused by the misalignment of strains with the fiber directions of the underlying fabric. This approach produced quad-like segments which were flattened to the plane and used as a design plan for stitching the formwork together. Our results demonstrated a reduction in large deformations and a closer match to the target shape.

8.1. Limitations and Future Work

Table 1 shows that most of the segmentation time is spent on running the dynamic, non-linear isotropic cloth simulation. Replacing it with a static solver and porting the simulation to the GPU could significantly reduce runtime and improve the efficiency of

our pipeline. While our approach effectively minimizes deformation, certain areas—such as the head of the child in the fertility model (Fig. 10, bottom row)—do not fully preserve their intended roundness. Similarly, the trunk in the elephant model isn't as arched as it should be (Fig. 14, middle row). Incorporating reinforcements into the formwork to increase rigidity in such regions for improved fidelity to the target shape is an exciting avenue for future work. Taking the effect of seams into account to inform a better segmentation would also be an interesting direction to work on. Since seams are inherently stiffer than the base fabric, they have a bigger impact on the deformation the mold will experience from the fluid infill.

We envision several enhancements that could further improve our design and manufacturing process. Our current 2D patch orientation approach uses simple heuristics, and could be improved by solving a global 1D optimization problem that yields the best overall alignment between patches and the strain field. Our formwork is stitched together with segments made from a single material. A more versatile approach would combine fabrics of varying stiffness—flexible materials to reduce wrinkling and conform to curvature, and stiffer ones with reinforcements to capture intricate geometries. Utilizing whole-garment 3D knitting [NAH*18] and 3D weaving techniques [MBFL99], which are already employed in creating near-net shapes for composite structures and for fabricating thin-shell concrete structures [PRL*21], could significantly speed up fabrication. However, this approach introduces new challenges, such as the need for waterproofing and dealing with the volume limitations imposed by machine specifications.

Acknowledgments

References

[AJL*19] ARORA R., JACOBSON A., LANGLOIS T. R., HUANG Y., MUELLER C., MATUSIK W., SHAMIR A., SINGH K., LEVIN D. I.: Volumetric michell trusses for parametric design & fabrication. In *Proceedings of the 3rd Annual ACM Symposium on Computational Fabrication* (2019), pp. 1–13. 3, 4

[AMA*22] ALDERIGHI T., MALOMO L., AUZINGER T., BICKEL B., CIGNONI P., PIETRONI N.: State of the art in computational mould design. In *Computer Graphics Forum* (2022), vol. 41, Wiley Online Library, pp. 435–452. 3

[AMB*21] ALDERIGHI T., MALOMO L., BICKEL B., CIGNONI P., PIETRONI N.: Volume decomposition for two-piece rigid casting. *ACM Trans. Graph. 40*, 6 (2021), 272–1. 3

[AMG*18] ALDERIGHI T., MALOMO L., GIORGI D., PIETRONI N., BICKEL B., CIGNONI P.: Metamolds: computational design of silicone molds. *ACM Transactions on Graphics (ToG) 37*, 4 (2018), 1–13. 2

[AMG*19] ALDERIGHI T., MALOMO L., GIORGI D., BICKEL B., CIGNONI P., PIETRONI N.: Volume-aware design of composite molds. *ACM Transactions on Graphics* (2019). 1

[Bog13] BOGUE R.: 3d printing: the dawn of a new era in manufacturing? *Assembly Automation 33*, 4 (2013), 307–311. 2

[BPT*25] BAHARAMI H., PIOVARCI M., TARINI M., BICKEL B., PIETRONI N.: Fabricable discretized ruled surfaces. *ACM Transactions on Graphics 44*, 3 (2025), 1–15. 3

[BW23] BARAFF D., WITKIN A.: Large steps in cloth simulation. In *Seminal Graphics Papers: Pushing the Boundaries, Volume 2*. 2023, pp. 767–778. 4

[BZK09] BOMMES D., ZIMMER H., KOBBELT L.: Mixed-integer quadrangulation. *ACM Transactions On Graphics (TOG) 28*, 3 (2009), 1–10. 5

[Cam17] CAMPEN M.: Partitioning surfaces into quadrilateral patches: A survey. In *Computer graphics forum* (2017), vol. 36, Wiley Online Library, pp. 567–588. 3, 6

[CSAD04] COHEN-STEINER D., ALLIEZ P., DESBRUN M.: Variational shape approximation. In *ACM SIGGRAPH 2004 Papers*. 2004, pp. 905–914. 7

[CZK15] CHOI S., ZHOU Q.-Y., KOLTUN V.: Robust reconstruction of indoor scenes. In *Proceedings of the IEEE Conference on Computer Vision and Pattern Recognition (CVPR)* (June 2015). 8

[FWYX24] FENG X., WANG H., YANG Y., XU W.: Neural-assisted homogenization of yarn-level cloth. In *SIGGRAPH 2024 Conference Papers* (New York, NY, USA, jul 2024), Association for Computing Machinery. 2

[Gor09] GORDON J. E.: *Structures: or why things don't fall down*. Da Capo Press, 2009. 2

[GSA*20] GROEN J. P., STUTZ F. C., AAGE N., BÆRENTZEN J. A., SIGMUND O.: De-homogenization of optimal multi-scale 3d topologies. *Computer Methods in Applied Mechanics and Engineering 364* (2020), 112979. 3

[GSV*17] GORI G., SHEFFER A., VINING N., ROSALES E., CARR N., JU T.: Flowrep: Descriptive curve networks for free-form design shapes. *ACM Transactions on Graphics (TOG) 36*, 4 (2017), 1–14. 3

[IRHSH20] ION A., RABINOVICH M., HERHOLZ P., SORKINE-HORNUNG O.: Shape approximation by developable wrapping. *ACM Transactions on Graphics (TOG) 39*, 6 (2020), 1–12. 3

[JKS05] JULIUS D., KRAEVOY V., SHEFFER A.: D-charts: Quasi-developable mesh segmentation. In *Computer Graphics Forum* (2005), vol. 24, Citeseer, pp. 581–590. 8

[JSVB22] JOURDAN D., SKOURAS M., VOUGA E., BOUSSEAU A.: Computational design of self-actuated surfaces by printing plastic ribbons on stretched fabric. In *Computer Graphics Forum* (2022), vol. 41, Wiley Online Library, pp. 493–506. 2

[KE20] KIM T., EBERLE D.: Dynamic deformables: implementation and production practicalities. In *ACM SIGGRAPH 2020 Courses*. 2020, pp. 1–182. 4

[Kho04] KHOSHNEVIS B.: Automated construction by contour crafting—related robotics and information technologies. *Automation in construction 13*, 1 (2004), 5–19. 2

[LCBD*18] LY M., CASATI R., BERTAILS-DESCOUBES F., SKOURAS M., BOISSIEUX L.: Inverse elastic shell design with contact and friction. *ACM Transactions on Graphics (TOG) 37*, 6 (2018), 1–16. 2

[LCK21] LYON M., CAMPEN M., KOBBELT L.: Simpler quad layouts using relaxed singularities. In *Computer Graphics Forum* (2021), vol. 40, Wiley Online Library, pp. 169–180. 3, 6

[LDW*22] LI Y., DU T., WU K., XU J., MATUSIK W.: Diffcloth: Differentiable cloth simulation with dry frictional contact. *ACM Transactions on Graphics (TOG) 42*, 1 (2022), 1–20. 2

[LLK19] LIANG J., LIN M., KOLTUN V.: Differentiable cloth simulation for inverse problems. *Advances in Neural Information Processing Systems 32* (2019). 2

[Lov13] LOVE A. E. H.: *A treatise on the mathematical theory of elasticity*. Cambridge university press, 2013. 3

[MBFL99] MOURITZ A. P., BANNISTER M. K., FALZON P., LEONG K.: Review of applications for advanced three-dimensional fibre textile composites. *Composites Part A: applied science and manufacturing 30*, 12 (1999), 1445–1461. 11

[MBT*12] MIGUEL E., BRADLEY D., THOMASZEWSKI B., BICKEL B., MATUSIK W., OTADUY M. A., MARSCHNER S.: Data-driven estimation of cloth simulation models. In *Computer Graphics Forum* (2012), vol. 31, Wiley Online Library, pp. 519–528. 2

[MPBC16] MALOMO L., PIETRONI N., BICKEL B., CIGNONI P.: Flex-molds: Automatic design of flexible shells for molding. *ACM Transactions on Graphics (TOG) 35*, 6 (2016), 1–12. 1

[MS04] MITANI J., SUZUKI H.: Making papercraft toys from meshes using strip-based approximate unfolding. *ACM transactions on graphics (TOG) 23*, 3 (2004), 259–263. 3

[MTMP20] MONTES J., THOMASZEWSKI B., MUDUR S., POPA T.: Computational design of skintight clothing. *ACM Transactions on Graphics (TOG) 39*, 4 (2020), 105–1. 2

[NAH*18] NARAYANAN V., ALBAUGH L., HODGINS J., COROS S., MCCANN J.: Automatic machine knitting of 3d meshes. *ACM Trans. Graph. 37*, 3 (Aug. 2018), 35:1–35:15. 11

[NJW01] NG A., JORDAN M., WEISS Y.: On spectral clustering: Analysis and an algorithm. *Advances in neural information processing systems 14* (2001). 6

[Ogd97] OGDEN R. W.: *Non-Linear Elastic Deformations*. Dover, 1997. 5

[PDF*22] PIETRONI N., DUMERY C., FALQUE R., LIU M., VIDAL-CALLEJA T., SORKINE-HORNUNG O.: Computational pattern making from 3d garment models. *ACM Transactions on Graphics (TOG) 41*, 4 (2022), 1–14. 1, 2, 3, 7, 8

[POT17] PÉREZ J., OTADUY M. A., THOMASZEWSKI B.: Computational design and automated fabrication of kirchhoff-plateau surfaces. *ACM Transactions on Graphics (TOG) 36*, 4 (2017), 1–12. 2

[PPM*16] PIETRONI N., PUPPO E., MARCIAS G., SCOPIGNO R., CIGNONI P.: Tracing field-coherent quad layouts. In *Computer graphics forum* (2016), vol. 35, Wiley Online Library, pp. 485–496. 3, 6

[PRL*21] POPESCU M., RIPPMANN M., LIEW A., REITER L., FLATT R. J., VAN MELE T., BLOCK P.: Structural design, digital fabrication and construction of the cable-net and knitted formwork of the knitcandela concrete shell. In *Structures* (2021), vol. 31, Elsevier, pp. 1287–1299. 11

[PTP*15] PIETRONI N., TONELLI D., PUPPO E., FROLI M., SCOPIGNO R., CIGNONI P.: Statics aware grid shells. In *Computer Graphics Forum* (2015), vol. 34, Wiley Online Library, pp. 627–641. 3

[RBB09] RUSU R. B., BLODOW N., BEETZ M.: Fast Point Feature Histograms (FPFH) for 3D Registration. In *Proceedings of the IEEE International Conference on Robotics and Automation (ICRA), Kobe, Japan, May 12-17* (2009). 8

[SB10] SCHIFTNER A., BALZER J.: Statics-sensitive layout of planar quadrilateral meshes. In *Advances in architectural geometry 2010*. Springer, 2010, pp. 221–236. 3

[SC17] SAWHNEY R., CRANE K.: Boundary first flattening. *ACM Transactions on Graphics (ToG) 37*, 1 (2017), 1–14. 7

[SC18] SHARP N., CRANE K.: Variational surface cutting. *ACM Trans. Graph. 37*, 4 (2018). 2, 7

[SC20] SHARP N., CRANE K.: You can find geodesic paths in triangle meshes by just flipping edges. *ACM Transactions on Graphics (TOG) 39*, 6 (2020), 1–15. 6

[SGC18] STEIN O., GRINSPUN E., CRANE K.: Developability of triangle meshes. *ACM Transactions on Graphics (TOG) 37*, 4 (2018), 1–14. 3, 6

[SJG19] STEIN O., JACOBSON A., GRINSPUN E.: Interactive design of castable shapes using two-piece rigid molds. *Computers & Graphics 80* (2019), 51–62. 3

[SOG*22] STUTZ F. C., OLSEN T. F., GROEN J. P., TRUNG T. N., AAGE N., SIGMUND O., SOLOMON J., BÆRENTZEN J. A.: Synthesis of frame field-aligned multi-laminar structures. *ACM Transactions on Graphics (TOG) 41*, 5 (2022), 1–20. 3

[SSBL*22] SPERL G., SÁNCHEZ-BANDERAS R. M., LI M., WOJTAN C., OTADUY M. A.: Estimation of yarn-level simulation models for production fabrics. *ACM Transactions on Graphics (TOG) 41*, 4 (2022), 1–15. 4

[VCD*16] VAXMAN A., CAMPEN M., DIAMANTI O., PANOZZO D., BOMMES D., HILDEBRANDT K., BEN-CHEN M.: Directional field synthesis, design, and processing. In *Computer graphics forum* (2016), vol. 35, Wiley Online Library, pp. 545–572. 4, 6

[VL07] VON LUXBURG U.: A tutorial on spectral clustering. *Statistics and computing 17* (2007), 395–416. 6

[VLAR19] VALKENEERS T., LEEN D., ASHBROOK D., RAMAKERS R.: Stackmold: Rapid prototyping of functional multi-material objects with selective levels of surface details. In *Proceedings of the 32nd Annual ACM Symposium on User Interface Software and Technology* (2019), pp. 687–699. 2

[VWB11] VEENENDAAL D., WEST M., BLOCK P.: History and overview of fabric formwork: using fabrics for concrete casting. *Structural Concrete 12*, 3 (2011), 164–177. 2

[VZF*19] VEKHTER J., ZHUO J., FANDINO L. F. G., HUANG Q., VOUGA E.: Weaving geodesic foliations. *ACM Transactions on Graphics (TOG) 38*, 4 (2019), 1–22. 3

[Wan07] WANG C.: Computing length-preserved free boundary for quasi-developable mesh segmentation. *IEEE Transactions on Visualization and Computer Graphics 14*, 1 (2007), 25–36. 3, 7

[Wes16] WEST M.: *The fabric formwork book: Methods for building new architectural and structural forms in concrete*. Routledge, 2016. 2

[WOR11] WANG H., O'BRIEN J. F., RAMAMOORTHI R.: Data-driven elastic models for cloth: modeling and measurement. *ACM transactions on graphics (TOG) 30*, 4 (2011), 1–12. 2, 9

[WZZ*23] WU K., ZHAO Z.-Y., ZHANG Z., LIU L., FU X.-M.: Piecewise developable modeling via implicit neural deformation and feature-guided cutting. *IEEE Transactions on Visualization and Computer Graphics* (2023). 3

[ZFO*22] ZHAO Z.-Y., FANG Q., OUYANG W., ZHANG Z., LIU L., FU X.-M.: Developability-driven piecewise approximations for triangular meshes. *ACM Transactions on Graphics (TOG) 41*, 4 (2022), 1–13. 3

[ZFS*19] ZHANG X., FANG G., SKOURAS M., GIESELER G., WANG C. C., WHITING E.: Computational design of fabric formwork. *ACM Transactions on Graphics 38*, 4 (2019), 1–13. 1, 2, 4, 7, 9